

SPITZER MICROLENSING OF MOA-2016-BLG-231L : A COUNTER-ROTATING BROWN DWARF BINARY IN THE GALACTIC DISK

SUN-JU CHUNG^{1,2,31}, ANDREW GOULD^{1,3,4,31,33}, JAN SKOWRON^{5,32}, IAN A. BOND^{6,34}, WEI ZHU^{7,33}

AND

MICHAEL D. ALBROW⁸, YOUNG KIL JUNG¹, CHEONGHO HAN⁹, KYU-HA HWANG¹, YOON-HYUN RYU¹, IN-GU SHIN¹⁰,
YOSSI SHVARTZVALD^{11,33}, JENNIFER C. YEE^{10,33}, WEICHENG ZANG¹², SANG-MOK CHA^{1,13}, DONG-JIN KIM¹,
HYOUN-WOO KIM¹, SEUNG-LEE KIM^{1,2}, YUN-HAK KIM^{1,2}, CHUNG-UK LEE^{1,2}, DONG-JOO LEE¹, YONGSEOK LEE^{1,13},
BYEONG-GON PARK^{1,2}, RICHARD W. POGGE³

(THE KMTNET COLLABORATION)

ANDRZEJ UDALSKI⁵, RADEK POLESKI^{3,5}, PRZEMEK MRÓZ⁵, PAWEŁ PIETRUKOWICZ⁵, MICHAŁ K. SZYMAŃSKI⁵,
IGOR SOSZYŃSKI⁵, SZYMON KOZŁOWSKI⁵, KRZYSZTOF ULACZYK^{5,14}, MICHAŁ PAWLAK⁵

(THE OGLE COLLABORATION)

CHARLES A. BEICHMAN¹⁵, GEOFFERY BRYDEN¹⁶, SEBASTIANO CALCHI NOVATI¹¹, SEAN CAREY¹⁷, B. SCOTT GAUDI³,
CALEN B. HENDERSON¹¹

(THE *Spitzer* TEAM)

FUMIO ABE¹⁸, RICHARD BARRY¹⁹, DAVID P. BENNETT^{19,20}, APARNA BHATTACHARYA^{19,20}, MARTIN DONACHIE²¹,
AKIHIKO FUKUI^{22,23}, YUKI HIRAO²⁴, YOSHITAKA ITOW¹⁸, KOHEI KAWASAKI²⁴, IONA KONDO²⁴, NAOKI KOSHIMOTO^{25,26},
MAN CHEUNG ALEX LI²¹, YUTAKA MATSUBARA¹⁸, YASUSHI MURAKI¹⁸, SHOTA MIYAZAKI²⁴, MASAYUKI NAGAKANE²⁴,
CLÉMENT RANC¹⁹, NICHOLAS J. RATTENBURY²¹, HARUNO SUEMATSU²⁴, DENIS J. SULLIVAN²⁷, TAKAHIRO SUMI²⁴,
DAISUKE SUZUKI²⁸, PAUL J. TRISTRAM²⁹, ATSUNORI YONEHARA³⁰

(THE MOA COLLABORATION)

¹ Korea Astronomy and Space Science Institute, 776 Daedeokdae-ro, Yuseong-Gu, Daejeon 34055, Korea; sjchung@kasi.re.kr

² Korea University of Science and Technology, 217 Gajeong-ro, Yuseong-gu, Daejeon 34113, Korea

³ Department of Astronomy, Ohio State University, 140 W. 18th Ave., Columbus, OH 43210, USA

⁴ Max-Planck-Institute for Astronomy, Königstuhl 17, 69117 Heidelberg, Germany

⁵ Warsaw University Observatory, Al. Ujazdowskie 4, 00-478 Warszawa, Poland

⁶ Institute of Natural and Mathematical Science, Massey University, Auckland 0745, New Zealand

⁷ Canadian Institute for Theoretical Astrophysics, 60 St George Street, University of Toronto, Toronto, ON M5S 3H8, Canada

⁸ Department of Physics and Astronomy, University of Canterbury, Private Bag 4800 Christchurch, New Zealand

⁹ Department of Physics, Chungbuk National University, Cheongju 361-763, Korea

¹⁰ Harvard-Smithsonian Center for Astrophysics, 60 Garden St., Cambridge, MA 02138, USA

¹¹ IPAC, Mail Code 100-22, Caltech, 1200 E. California Blvd., Pasadena, CA 91125, USA

¹² Physics Department and Tsinghua Centre for Astrophysics, Tsinghua University, Beijing 100084, People's Republic of China

¹³ School of Space Research, Kyung Hee University, Giheung-gu, Yongin, Gyeonggi-do, 17104, Korea

¹⁴ Department of Physics, University of Warwick, Gibbet Hill Road, Coventry, CV4 7AL, UK

¹⁵ NASA Exoplanet Science Institute, MS 100-22, California Institute of Technology, Pasadena, CA 91125, USA

¹⁶ Jet Propulsion Laboratory, California Institute of Technology, 4800, Oak Grove Dr., Pasadena, CA 91109, USA

¹⁷ Spitzer Science Center, MS 220-6, California Institute of Technology, Pasadena, CA, USA

¹⁸ Institute for Space-Earth Environmental Research, Nagoya University, Nagoya 464-8601, Japan

¹⁹ Code 667, NASA Goddard Space Flight Center, Greenbelt, MD 20771, USA

²⁰ Department of Astronomy, University of Maryland, College Park, MD 20742, USA

²¹ Department of Physics, University of Auckland, Private Bag 92019, Auckland, New Zealand

²² Subaru Telescope Okayama Branch Office, National Astronomical Observatory of Japan, NINS, 3037-5 Honjo, Kamogata, Asakuchi,

Okayama 719-0232, Japan

²³ Instituto de Astrofísica de Canarias, Vía Láctea s/n, E-38205 La Laguna, Tenerife, Spain

²⁴ Department of Earth and Space Science, Graduate School of Science, Osaka University, Toyonaka, Osaka 560-0043, Japan

²⁵ Department of Astronomy, Graduate School of Science, The University of Tokyo, 7-3-1 Hongo, Bunkyo-ku, Tokyo 113-0033, Japan

²⁶ National Astronomical Observatory of Japan, 2-21-1 Osawa, Mitaka, Tokyo 181-8588, Japan

²⁷ School of Chemical and Physical Science, Victoria University, Wellington, New Zealand

²⁸ Institute of Space and Astronautical Science, Japan Aerospace Exploration Agency, Kanagawa 252-5210, Japan

²⁹ University of Canterbury Mt. John Observatory, P.O.Box 56, Lake Tekapo 8770, New Zealand

³⁰ Department of Physics, Faculty of Science, Kyoto Sangyo University, Kyoto 603-8555, Japan

³¹ The KMTNet Collaboration

³² The OGLE Collaboration

³³ The *Spitzer* Team and

³⁴ The MOA Collaboration

Draft version February 13, 2019

ABSTRACT

We analyze the binary microlensing event MOA-2016-BLG-231, which was observed from the ground and from *Spitzer*. The lens is composed of very low-mass brown dwarfs (BDs) with $M_1 = 21_{-5}^{+12} M_J$ and $M_2 = 9_{-2}^{+5} M_J$, and it is located in the Galactic disk $D_L = 2.85_{-0.50}^{+0.88}$ kpc. This is the fifth binary brown dwarf discovered by microlensing, and the BD binary is moving counter to the orbital motion of disk stars. Constraints on the lens physical properties come from late time, non-caustic-crossing features of the *Spitzer* light curve. Thus, MOA-2016-BLG-231 shows how *Spitzer* plays a crucial role in resolving the nature of BDs in binary BD events with short timescale ($\lesssim 10$ days).

Keywords: binaries: general - brown dwarfs - gravitational lensing: micro

1. INTRODUCTION

Brown dwarfs (BDs) are substellar objects that are not massive enough to burn hydrogen. BDs have a mass between gas giant planets and low-mass stars, and it is thought that the formation and evolution of BDs are different from those of planets and stars (Ranc et al. 2015). Thus, studying BDs is helpful to understand the formation and evolution of stars and planets.

Microensing is an excellent method to detect faint low-mass objects, such as BDs and planets because it does not depend on the light from the objects, but the mass. Until now 32 BDs have been detected by microensing. Only five of these are isolated BDs, while all the others belong to binary systems. Microensing BDs are mostly binary companions to faint M dwarf stars (see Table 1), while most of the many BDs detected by the radial velocity, transit, and direct imaging methods are companions to solar-type stars (Ranc et al. 2015). Hence, microensing BDs are important to constrain BD formation scenarios including turbulent fragmentation of molecular clouds (Boyd & Whitworth 2005), fragmentation of unstable accretion disks (Stamatellos et al. 2007), ejection of protostars from prestellar cores (Reipurth & Clarke 2001), and photo-erosion of prestellar cores by nearby very bright stars (Whitworth & Zinnecker 2004).

However, with microensing, it is generally difficult to measure the mass of a lens. This is because we usually obtain only the Einstein timescale,

$$t_E \equiv \frac{\theta_E}{\mu_{\text{rel}}}, \quad (1)$$

where θ_E is the angular Einstein radius corresponding to the total lens mass and μ_{rel} is the relative lens-source proper motion. For the measurement of the lens mass, one needs to measure the angular Einstein radius and microlens parallax π_E , which yields

$$M_L = \frac{\theta_E}{\kappa\pi_E}, \quad \theta_E^2 = \kappa M_L \pi_{\text{rel}}, \quad (2)$$

where $\pi_{\text{rel}} \equiv \text{au}(D_L^{-1} - D_S^{-1})$ is the lens-source relative parallax, D_L and D_S are the distances to the lens and source, respectively, and $\kappa \equiv 4G/(c^2\text{au}) \approx 8.14 \text{ mas}/M_\odot$ (Gould 2000). The angular Einstein radius can be measured from events with finite-source effects, while the microlens parallax can be measured from the detection of light-curve distortions induced by the orbital motion of Earth on a standard microensing light curve (Gould 1992, 2013). The large number of microensing BDs detected to date would appear to indicate that M dwarf-BD binaries and BD binaries are very common. This is because their mass measurements (hence, unambiguous determination that they are BDs) require clear detection of a microlens parallax signal that can be detected from the ground despite a relatively short timescale. However, it is usually very difficult to measure the microlens parallax, especially for short timescale events, such as M dwarf-BD binaries. While the microensing parallax (derived from Equation(2))(Gould 2000)

$$\pi_E = \sqrt{\frac{\pi_{\text{rel}}}{\kappa M_L}} \quad (3)$$

is on average large for low-mass lenses, this is not by itself usually sufficient to render it measurable in short events. Rather, large π_{rel} is required as well. As a result, half (7/13) of microensing binaries containing at least one BD and with mass measurements based on ground-based microensing parallaxes have distances $D_L \lesssim 2 \text{ kpc}$, which would be true of a tiny fraction of all microensing events. Moreover, of the remainder, all lie in the Galactic disk $D_L < 5 \text{ kpc}$, and almost all have low, or very low proper motions (so long, or very long timescales), which again is rare.

Hence, it is important to check independently that these relatively frequent detections are not just due to systematics misinterpreted as ‘‘parallax signal’’. The *Spitzer* satellite allows us to do that. *Spitzer* observations together with ground-based observations yield the microensing parallax, which does not depend strongly on the event timescale and lens distance. Thus, *Spitzer* makes it possible to measure the masses of the lenses in short t_E binary BD events, which would be quite difficult using only ground-based observations. The microlens parallax is measured from the difference in the light curves as seen from the two observatories with wide projected separation D_\perp (Refsdal S. 1966; Gould 1994), which is represented by

$$\pi_E \simeq \frac{\text{au}}{D_\perp} (\Delta\tau, \Delta\beta_{\pm\pm}), \quad (4)$$

where

$$\Delta\tau = \frac{t_{0,\text{sat}} - t_{0,\oplus}}{t_E}; \quad \Delta\beta_{\pm\pm} = \pm u_{0,\text{sat}} - \pm u_{0,\oplus}, \quad (5)$$

and where the subscripts indicate the parameters as measured from the satellite and Earth. Here t_0 is the time of the closest source approach to the lens (peak time of the event) and u_0 is the separation between the lens and the source at time t_0 .

In this paper, we report the discovery of the fifth binary BD from the analysis of the microensing event MOA-2016-BLG-231, which was observed from the ground and from *Spitzer*. Although *Spitzer* can identify binary BDs

events with short t_E , observing such events is extremely challenging because of the short timescale and the 3 – 9 day observation delay (see Figure 1 of Udalski et al. 2015). Thus, *Spitzer* does not usually observe caustic crossings of such events. However, we here show that even non caustic-crossing *Spitzer* light curves can resolve the nature of a binary BD lens.

2. OBSERVATIONS

2.1. Ground-based observations

The microlensing event MOA-2016-BLG-231 was first alerted on UT 22:18 6 May by the Microlensing Observations in Astrophysics (MOA; Suzuki et al. 2016). MOA uses a 1.8 m telescope with 2.2 deg² field-of-view (FOV) at Mt. John Observatory in New Zealand. The lensed source star is at $(\alpha, \delta)_{J2000} = (17^{\text{h}}53^{\text{m}}12^{\text{s}}.0, -30^{\circ}11'32''.1)$, corresponding to $(l, b) = (359^{\circ}.77, -2^{\circ}.06)$. The Early Warning System (EWS) of the Optical Gravitational Lensing Experiment (OGLE) collaboration (Udalski A. 2003) also alerted this event 7 days after the MOA alert. OGLE uses the 1.3 m Warsaw telescope at the Las Campanas Observatory in Chile. The event is located in the OGLE field BLG501, which is observed with cadence $\Gamma \simeq 0.4 \text{ hr}^{-1}$. The event is designated as OGLE-2016-BLG-0864 by OGLE. Here we note that although MOA first alerted the event, *Spitzer* observations were triggered by OGLE data rather than MOA, and MOA did not play a major role in characterization of the lens. Since the Einstein crossing time of the event is short $t_E \sim 13$ days, and the OGLE baseline is slightly variable on long timescales, we used only 2016 season data sets of OGLE and MOA for light curve modeling.

The event was also observed by the Korea Microlensing Telescope Network (KMTNet; Kim et al. 2016). KMTNet uses 1.6 m telescopes with 4.0 deg² FOV at CTIO in Chile (KMTC), SAAO in South Africa (KMTS), and SSO in Australia (KMTA). MOA-2016-BLG-231 lies in two overlapping KMTNet fields, BLG01 and BLG42, with a combined cadence of $\Gamma = 4 \text{ hr}^{-1}$. It is designed by KMTNet as KMT-2016-BLG-0285 (Kim et al. 2018). Most of KMTNet data were taken in *I* band, and for the characterization of the source star, some data were taken in *V* band from CTIO. The KMTNet data were reduced by pySIS based on the difference imaging method (Alard & Lupton 1998; Albrow et al. 2009).

2.2. Spitzer observations

Since 2014, *Spitzer* has been observing microlensing events toward the Galactic bulge in order to measure the microlens parallax. While the overwhelming majority of events chosen for *Spitzer* observations are (apparently) generated by point-mass lenses at the time of selection, in accordance with the detailed protocols described by Yee et al. (2015), the *Spitzer* team does select known binary and planetary lenses whenever there appears to be a reasonable chance to measure the microlens parallax. MOA-2016-BLG-231 was such a case. At the time of selection, the event was regarded by the team as “difficult, but maybe doable” because it was recognized that the timescale of event was quite short and the first *Spitzer* observation would be 15 days after the final anomalous feature in the light curve. See Figure 1. It was observed for three weeks, mostly at a cadence of $\sim 1 \text{ day}^{-1}$, but roughly double that for the first few days because of the limited number of available events due to *Spitzer*’s sun-angle exclusion of more easterly targets.

3. LIGHT CURVE ANALYSIS

3.1. Ground-based data

The observed ground-based data of the event MOA-2016-BLG-231 have a clear caustic-crossing feature, while the *Spitzer* data (as anticipated) show only a general decline. We therefore begin by incorporating only ground-based data to conduct binary lens modeling. Standard binary lens modeling requires seven parameters including three single-lens parameters (t_0, u_0, t_E) and four additional parameters: the projected separation of the lens components in units of θ_E (s), the mass ratio of the components (q), the angle between the source trajectory and the binary axis (α), and the normalized source radius ($\rho = \theta_*/\theta_E$) (Rhie et al. 1999), where θ_* is the angular radius of the source. In addition, there are two flux parameters for each observatory, the source flux $f_{s,i}$ and blended flux $f_{b,i}$ of the i th observatory. The two flux parameters at a given time t_j are modeled by

$$F_i(t_j) = f_{s,i}A_i(t_j) + f_{b,i}, \quad (6)$$

where A_i is the magnification as a function of time at the i th observatory (Rhie et al. 1999). The two flux parameters of each observatory are determined from a linear fit.

We conduct a grid search in the parameter space (s, q, α) to find the best-fit model. The ranges of the parameters are $-1 \leq \log s \leq 1$, $-2 \leq \log q \leq 0$, and $0 \leq \alpha \leq 2\pi$, respectively. During the grid search, the other parameters are searched for using a Markov Chain Monte Carlo (MCMC) method. The magnification is calculated by inverse ray shooting near and in the caustic (Kayser et al. 1986; Schneider & Weiss 1988; Wambsganss 1997) and multipole approximations (Pejcha & Heyrovský 2009; Gould 2008) otherwise. From this, we find only one local minimum at $(s, q, \alpha) \simeq (1.3, 0.4, 4.2)$. We then seed the local solutions into the MCMC for which all parameters are allowed to vary, and finally find a global solution of the binary lens model.

As in many binary and planetary events, ρ can be measured from the effect of the finite size of the source to smooth the intrinsically divergent magnification profile of the caustic. Because the source crosses the caustic, we consider the limb-darkening variation of the finite source star in the modeling. For this, we adopt the source brightness profile,

which is approximated by

$$S_\lambda = \frac{F_\lambda}{\pi\theta_*^2} \left[1 - \Gamma_\lambda \left(1 - \frac{3}{2} \cos \phi \right) \right], \quad (7)$$

where F_λ is the total flux of the source at wavelength λ , Γ_λ is the limb darkening coefficient, and ϕ is the angle between the normal to the surface of the source star and the line of sight (An et al. 2002). According to the source type, which is discussed in Section 4, we adopt that $\Gamma_I = 0.54$, $\Gamma_V = 0.711$, and $\Gamma_L = 0.178$ from Claret (2000) and Claret & Bloemen (2011).

3.2. Combination of ground-based and Spitzer data

Thanks to the *Spitzer* data, we can constrain the higher-order effects of microlensing parallax and lens orbital motion, even though $t_E \simeq 13$ days would not be long enough to detect these two effects using ground-based data alone. When including the parallax effect in the model, it is important to include also the orbital motion effect because of the degeneracy between the two (Skowron et al. 2011; Batista et al. 2011; Han et al. 2016). Thus, we conduct the modeling with both parallax and orbital effects. The microlens parallax enters as a two-parameter vector $\boldsymbol{\pi}_E = (\pi_{E,N}, \pi_{E,E})$, whose amplitude is given by Equation (4) and whose direction is that of the lens-source relative proper motion in the geocentric frame, i.e., $\boldsymbol{\pi}_E = \pi_E(\boldsymbol{\mu}/\mu)$. Under the approximation of linear orbital motion of the binary lens, the orbital motion effect is described by two parameters, ds/dt and $d\alpha/dt$, which are the change rates of the binary separation and the orientation angle of the binary axis, respectively. Hence, four additional parameters are added in the model. In contrast to the ground-based light curve, *Spitzer* covers only the falling wing of the light curve. Thus, it is essential to incorporate the color constraint between OGLE and *Spitzer* ($I_{\text{ogle}} - L$) in order to find the correct parallax solution. See, for example, the analysis of OGLE-2016-BLG-0168 by Shin et al. (2017). We find $(I_{\text{ogle}} - L) = 1.911 \pm 0.020$ by combining the source instrumental ($V - I$) color measurement, which is discussed in Section 4, with a *VIL* instrumental color-color relation derived from matched field stars. To enforce the color constraint, we add a χ_{penalty}^2 to χ^2 calculated in the model, which is defined as

$$\chi_{\text{penalty}}^2 = \frac{\{(I_{\text{ogle}} - L) + 2.5 \log(F_{s,\text{ogle}}/F_{s,\text{spitzer}})\}^2}{\sigma_c^2}, \quad (8)$$

where $F_{s,\text{ogle}}$ and $F_{s,\text{spitzer}}$ are the source fluxes of OGLE and *Spitzer*, which are obtained from the model, and σ_c is the error of the color constraint ($I_{\text{ogle}} - L$). Thus, $\chi_{\text{total}}^2 = \chi^2 + \chi_{\text{penalty}}^2$. In order to find correct source and blended fluxes of *Spitzer*, $F_{s,\text{spitzer}}$ and $F_{b,\text{spitzer}}$, with a strong color constraint, we include them as chain variables when modeling. Because of the low value of t_E , we expect most of the microlens parallax “signal” to come from *Spitzer* and not the ground-based data. However, we find that when we model the event using all data sets, most of these contribute signal at the $\Delta\chi^2$ of few tens level (and with different signs), with these signals coming overwhelmingly from the wings of the event, as determined from a cumulative $\Delta\chi^2$ plot (see further below). Such false parallax signals are not uncommon in MOA data, and have also been seen in KMTNet data during its much shorter history. Therefore, we restrict all ground-based data sets except OGLE to the time interval $7530.0 < \text{HJD}' < 7544.0$, where the rapid changes in magnification ensure that very low-level systematics will not play any significant role. We then find that the cumulative distribution of $\Delta\chi^2 = \chi_{\text{parallax+orbital}}^2 - \chi_{\text{standard}}^2$ shows no strong trends in any of the data sets except *Spitzer*. See Figure 2.

Observations from the ground and from *Spitzer* yield a well-known four degeneracy for the microlens parallax : $(+, +)$, $(+, -)$, $(-, +)$, and $(-, -)$, which register the signs of the impact parameters as measured from the ground and *Spitzer*, respectively (Zhu et al. 2015). From the modeling, we find that the event MOA-2016-BLG-231 has only two solutions, $(+, -)$ and $(-, -)$, and that the $(+, -)$ solution is preferred by $\Delta\chi^2 = 1.92$. The other models $(+, +)$ and $(-, +)$ converge to $(+, -)$ and $(-, -)$ models, respectively. The best-fit lensing parameters of the $(+, -)$ and $(-, -)$ models are presented in Table 2. Figure 1 shows the best-fit light curve of the event, i.e., for the $(+, -)$ model. The corresponding source trajectories for the ground and *Spitzer* are presented in Figure 3. Figure 3 also shows the caustic structures and positions of the lens components at three different epochs, $t_1 = 7531.9$ (caustic entrance), $t_2 = 7537.3$ (caustic exit), and $t_3 = 7570.0$ (close to baseline). As shown in Figure 3, the caustics and lens positions at the two epochs (t_1 and t_2) appear almost the same. This is because the characteristic orbital timescale, $\gamma^{-1} \simeq 1.0$ yr is long compared to the time interval explored $t_2 - t_1 \simeq 5$ days. Here, $\boldsymbol{\gamma} \equiv (\gamma_{\parallel}, \gamma_{\perp}) = (ds/dt/s, d\alpha/dt)$. While the χ^2 improvement of the parallax+orbital solution compared to the parallax-only solution is relatively small, $\Delta\chi^2 \simeq 9$, we will argue in Section 5 that this detection of orbital motion is likely real.

Figure 4 shows $\Delta\chi^2$ distributions of the parallax and orbital motion parameters for the $(+, -)$ and $(-, -)$ models. The parallax amplitude $\pi_E = |\boldsymbol{\pi}_E|$ is quite well constrained and very similar in the two cases, implying that the mass and distance of the system will be both well measured and not seriously impacted by the two-fold parallax degeneracy. From this, we find that even though *Spitzer* has no caustic-crossing features and it has only fragmentary coverage of the light curve, we can constrain the physical properties of lens.

In Figure 4, we mark four representative models for $(+, -)$, which are located just inside the 3σ contour. The corresponding parallax and orbital parameters are presented in Table 2. Figure 5 shows the *Spitzer* trajectories and resulting light curves of the four models. As shown in Figure 5, these four models have different trajectories from the best-fit one, and hence dramatically different predicted *Spitzer* light curves over the peak of the event. However,

during the time interval that *Spitzer* actually took data, all four predict similar light curves (see the inset to Figure 5). Despite these different trajectories, and as discussed above, these have qualitatively similar amplitudes, π_E , which is what enables a mass measurement.

4. ESTIMATE OF θ_E

As mentioned in Section 1, θ_E and π_E should be measured for the measurements of the mass and distance of the lens. Thanks to caustic-crossing features, one measure ρ from the modeling, while $\theta_E = \theta_\star/\rho$. Thus, we need to estimate θ_\star for the measurement of θ_E . We estimate θ_\star from the intrinsic color and brightness of the source, which can be derived by the offset between the source and the red clump in the instrumental color and magnitude diagram (CMD) (see Fig. 6) (Yoo et al. 2004). These are determined by

$$[(V - I), I]_{s,0} = [(V - I), I]_{\text{clump},0} + [\Delta(V - I), \Delta I], \quad (9)$$

where $[\Delta(V - I), \Delta I]$ is the offsets of the color and brightness between the source and the clump. We determine the instrumental source color by regression of the V on I flux measurements and derive the source instrumental magnitude from the model. These have errors of 0.004 and 0.020 mag, respectively. We then centroid the clump in color and magnitude with errors of 0.022 and 0.05 mag respectively. The measured color and magnitude offsets are $[\Delta(V - I), \Delta I] = [0.06 \pm 0.02, -0.19 \pm 0.05]$. Adopting $[(V - I), I]_{\text{clump},0} = (1.06, 14.44)$ from Bensby et al. (2011) and Nataf et al. (2013), we find $[(V - I), I]_{s,0} = [1.12, 14.25]$. This indicates that the source is a K-type giant. We determine the angular radius of the source θ_\star using *VIK* color-color relation (Bessell & Brett 1988) and the color/surface brightness relation (Kervella et al. 2004). As a result, we find that $\theta_\star = 7.23 \pm 0.40 \mu\text{as}$. With the measured ρ and θ_\star , we determine the angular radius of the Einstein ring corresponding to the total mass of the lens,

$$\theta_E = \theta_\star/\rho = 0.233_{-0.014}^{+0.013} \text{ mas}. \quad (10)$$

The relative lens-source proper motion is

$$\mu_{\text{rel}} = \theta_E/t_E = 6.57 \pm 0.37 \text{ mas yr}^{-1}. \quad (11)$$

5. LENS PROPERTIES

Using the estimated θ_E and $\pi_E = 0.99_{-0.35}^{+0.31}$, we measure the total mass of the lens system,

$$M = \frac{\theta_E}{\kappa\pi_E} = 0.029_{-0.007}^{+0.016} M_\odot.$$

The lens is composed of low-mass BDs with masses $M_1 = 0.020_{-0.005}^{+0.011} M_\odot$ and $M_2 = 0.009_{-0.002}^{+0.005} M_\odot$, where $M = M_1 + M_2$, and the projected separation of the two BDs is $a_\perp = 0.88_{-0.15}^{+0.27}$ au. The relative parallax between the lens and the source is

$$\pi_{\text{rel}} = \theta_E\pi_E = 0.23_{-0.08}^{+0.07} \text{ mas}. \quad (12)$$

Assuming that the source is located at 8.3 kpc (Nataf et al. 2013), we estimate the distance to the lens,

$$D_L = \left(\frac{\pi_{\text{rel}}}{\text{au}} + \frac{1}{D_S} \right)^{-1} = 2.85_{-0.50}^{+0.88} \text{ kpc}. \quad (13)$$

Hence, the lens is a BD binary located in the Galactic disk. This is the fourth BD binary discovered by microlensing. Because θ_E is well measured due to a precise ρ measurement, which comes from good coverage of caustic-crossing, the errors in the mass and distance of the lens primarily reflect the error in π_E . As shown in Figure 4, the correlation between $\pi_{E,N}$ and $\pi_{E,E}$ components is not well approximated by a linear relation. Hence, we use the best-fit MCMC chains to determine the errors in physical lens parameters including the mass and distance of the lens. Then, one can determine the standard deviation of each physical parameter from the chains. Thus, physical lens parameters in Table 3 represent the median values of each physical parameter from the (+, -) and (-, -) MCMC chains, and their error bars represent the 16th and 84th percentile values of each parameter from the chains.

In order to check that the binary lens is a bound system, we compute β , i.e., the ratio of the projected kinetic to potential energy (An et al. 2002),

$$\beta \equiv \left(\frac{\text{KE}}{\text{PE}} \right)_\perp = \frac{(s\theta_E D_L/\text{au})^3 (\gamma^2 \text{ yr}^2)}{M/M_\odot} = 0.16_{-0.10}^{+0.20} \quad (14)$$

where $\gamma = [(ds/dt/s)^2 + (d\alpha/dt)^2]^{1/2}$. Since $\beta = 0.16_{-0.10}^{+0.20}$ (or $\beta = 0.52_{-0.21}^{+0.30}$ for (-, -) model) represents very typical values for a bound pair seen at random orientation, and in particular indicates that the lens system satisfies the condition of a bound system, $\beta < 1$ (An et al. 2002), it is valid. We list estimated physical parameters of the lens system in Table 3. In Table 3, we also list physical lens parameters for four models with $\Delta\chi^2 \sim 9$ from Figures 4 & 5. Three of the four models imply that the lens system is a low-mass BD binary in the disk, similar to the best-fit solutions, while for model 1 it is a binary composed of a low-mass star and a BD in the disk. This is because of large uncertainties of $\pi_{E,N}$, as shown in Figure 4. We further discuss these models of the lens system in Section 6.

6. DISCUSSION

Table 2 shows that all $\pi_{E,E}$ for two best models is negative. This means that the lens located in the Galactic disk is moving in the opposite direction to the disk orbital motion. It is unusual. In order to check that it is real, we conduct the modeling under the condition that high-order effect parameters set to zero and the initial values of the other standard model parameters including *Spitzer* fluxes set to the best-fit solutions of the two parallax+orbital models including $(+, -)$ and $(-, -)$. We also conduct the same test for the four models indicated in Figure 4. As a result, we find that for all of the six models the slope of the *Spitzer* fluxes is steeper than the model (see Figure 7). This means that *Spitzer* observed the event later than Earth, and the lens is moving toward *Spitzer*, i.e., toward the west. Therefore, it is real that the lens is moving in the opposite direction to the disk orbital motion. In addition, in order to demonstrate that the lens is moving west relative to the source, we measure the proper motion of the source (see Figure 8). We find that $\boldsymbol{\mu}_S = (\mu_{S,N}, \mu_{S,E}) = (0.021 \pm 0.699, 0.231 \pm 0.699)$ mas yr $^{-1}$. As shown in Figure 8, the source is certainly part of the bulge population and is not moving relative to the bulge stars. Hence, the measurement of the lens-source relative motion clearly means that the lens is not moving with the disk. With the measurement of the source proper motion, we can measure the heliocentric proper motion of the lens,

$$\boldsymbol{\mu}_{L,\text{hel}} = \boldsymbol{\mu}_S + \boldsymbol{\mu}_{\text{rel}} + \frac{\pi_{\text{rel}}}{\text{au}} \mathbf{v}_{\oplus,\perp}, \quad (15)$$

where $\mathbf{v}_{\oplus,\perp}$ is the velocity of Earth at the peak of the event and projected perpendicular to the directory of the event. For this case, $\mathbf{v}_{\oplus,\perp} = (v_N, v_E) = (1.09, 26.89)$ km s $^{-1}$. From Equation (14), we find that $(\mu_{L,\text{hel},N}, \mu_{L,\text{hel},E}) = (-6.16_{-0.38}^{+0.40}, -0.37_{-0.39}^{+0.25})$ mas yr $^{-1}$ for $(+, -)$ solution, while for $(-, -)$ solution, $(\mu_{L,\text{hel},N}, \mu_{L,\text{hel},E}) = (-6.09_{-0.39}^{+0.43}, -0.87_{-0.74}^{+0.34})$ mas yr $^{-1}$. From the measurement of $\boldsymbol{\mu}_{L,\text{hel}}$, we can also measure the transverse velocity of the lens, (Shvartzvald et al. 2018),

$$\mathbf{v}_{L,\perp} = D_L \boldsymbol{\mu}_{L,\text{hel}} + \left(1 - \frac{D_L}{D_S}\right) \mathbf{v}_{\odot}, \quad (16)$$

where $\mathbf{v}_{\odot} = \mathbf{v}_{\odot,\text{pec}} + \mathbf{v}_{\odot,\text{cir}}$. Here $v_{\odot,\text{pec}}(l, b) = (12, 7)$ km s $^{-1}$ are the transverse components of the Sun's peculiar velocity relative to the Local Standard of Rest and $v_{\odot,\text{cir}}(l, b) = (220, 0)$ km s $^{-1}$ is the disk circular velocity. Thus, the peculiar velocity of the lens relative to the mean motion of the Galactic disk stars (Shvartzvald et al. 2018) is

$$\begin{aligned} \mathbf{v}_{L,\text{pec}} &= \mathbf{v}_{L,\perp} - \mathbf{v}_{L,\text{cir}} \\ &= D_L \boldsymbol{\mu}_{L,\text{hel}} - \mathbf{v}_{\odot,\text{cir}} \frac{D_L}{D_S} + \mathbf{v}_{\odot,\text{pec}} \left(1 - \frac{D_L}{D_S}\right), \end{aligned} \quad (17)$$

where $\mathbf{v}_{L,\text{cir}} = \mathbf{v}_{\odot,\text{cir}}$ because both lens and Sun are disk stars. From Equation (16), we find that for two degenerate solutions, $(+, -)$ and $(-, -)$, $v_{L,\text{pec}}(l, b) = (-144.12_{-50.40}^{+37.69}, -27.78_{-7.79}^{+5.95})$ km s $^{-1}$ and $v_{L,\text{pec}}(l, b) = (-172.29_{-66.15}^{+38.72}, -24.98_{-7.71}^{+7.17})$ km s $^{-1}$, respectively. This means that the lens is counter-rotating relative to the motion of Galactic disk stars. In order to check that the four models with $\Delta\chi^2 \sim 9$ in Figure 4 are compatible with the two solutions, we also estimate the proper motions and peculiar velocities of the lens for the four models, and they are as follows as

$$\begin{aligned} \mu_{L,\text{hel}}(N, E) &= \begin{cases} (-3.67, -5.03) \text{ mas yr}^{-1} & \text{for model 1} \\ (-6.35, -0.03) \text{ mas yr}^{-1} & \text{for model 2} \\ (-6.01, -0.72) \text{ mas yr}^{-1} & \text{for model 3} \\ (-5.87, -0.10) \text{ mas yr}^{-1} & \text{for model 4,} \end{cases} \\ v_{L,\text{pec}}(l, b) &= \begin{cases} (-331.79, 85.82) \text{ km s}^{-1} & \text{for model 1} \\ (-160.13, -38.37) \text{ km s}^{-1} & \text{for model 2} \\ (-129.25, -20.73) \text{ km s}^{-1} & \text{for model 3} \\ (-90.08, -18.29) \text{ km s}^{-1} & \text{for model 4.} \end{cases} \end{aligned}$$

The lens proper motions of the four models are consistent with those of the two best-fit solutions. Therefore, the lens is a counter-rotating disk object. Until now two counter-rotating disk objects (OGLE-2016-BLG-1195L (Shvartzvald et al. 2017), OGLE-2017-BLG-0896L (Shvartzvald et al. 2018)) have been discovered by microlensing, the first being right at the hydrogen-burning limit and the second being a low-mass BD. MOA-2016-BLG-231L is the third such object, and it is the first counter-rotating BD binary discovered by *Spitzer*. The unusual kinematics of the BD binary suggest that the BD binary could be a halo object or a member of counter-rotating low-mass object population, as mentioned in Shvartzvald et al. (2018).

For the event MOA-2016-BLG-231, it is found that there is an extremely small offset between the source position and the baseline object. The offset is 0.05 pixels, and it corresponds to 0.05×0.26 arcsec = 13 mas. This means that the blend could be associated with the event. However, the blended flux is in fact consistent with zero. First, the formal estimate of the blended flux is $f_b = 0.33 \pm 0.17$, where one unit of flux corresponds to $I = 18$. This in itself is consistent with zero at the 2σ level. Moreover, the estimate of f_b is ultimately derived from $f_b = f_{\text{base}} - f_s$, where f_s is the source flux from the microlensing model and f_{base} comes from DoPhot (Schechter et al. 1993) photometry of this field location. Because of the mottled background of unresolved turnoff stars in these crowded fields, f_{base} can easily

have errors at this level. Therefore, there is no clear evidence for blended light. In addition, we measure I_{base} using OGLE deep stack images. From this, we find that I_{base} from the deep stack images is 0.06 mag brighter than the value obtained from the OGLE reference images (i.e. normal OGLE data) due to a nearby star at $0.6''$. Hence, I_{base} cannot be estimated from the reference image photometry to better than 0.06 mag due to the presence of the nearby star. Therefore blended light cannot be determined better than 0.5 flux units. This reinforces the naive conclusion that there is no evidence for light from the lens.

The result of modeling with chain variables $F_{\text{s,spitzer}}$ and $F_{\text{b,spitzer}}$ yields negative $F_{\text{b,spitzer}}$ (see Table 2). $F_{\text{b,spitzer}} \sim -4.5$ (see Table 2). This is somewhat unusual. As reported in Calchi Novati et al. (2015) and Shvartzvald et al. (2018), the negative *Spitzer* blending can be generated when the flux of unresolved faint stars is included in the global background flux. The event OGLE-2017-BLG-0896 (Shvartzvald et al. 2018) is also the event affected by the excess flux due to unresolved stars and has almost the same *Spitzer* blending as this event.

The result of this study indicates that the lens system of MOA-2016-BLG-231 consists of two low-mass BDs. In principle, there are two scenarios that would drive us to very different conclusions, but neither of them is likely to be true. First, a smaller parallax value would give a more massive and more distant lens system. For example, out of the four models indicated in Figure 4, model 1 has the smallest parallax, which produces the most massive and the most distant lens system and thus might in principle solve the puzzle on the counter-rotating motion. However, the model 1 gives a low-mass M dwarf-BD binary with $M_{\text{tot}} = 0.18 M_{\odot}$ at a distance of $D_{\text{L}} = 6.3$ kpc, which still implies that it is in the disk. Moreover, with proper motion $\mu_{\text{L, hel}}(N, E) = (-3.7, -5.0)$, it is still counter-rotating. Therefore, the smaller parallax scenario is unlikely to resolve the issue of a counter-rotating lens. Furthermore, for the other models, all the lens systems are low-mass BD binaries with $M_{\text{tot}} = 0.02 \sim 0.03 M_{\odot}$ that is located at the disk $D_{\text{L}} < 3.2$ kpc and their proper motions are consistent with the two best-fit models (see Table 3), as mentioned before.

Another possibility could be that such an unusual solution arises from the unknown systematics in the *Spitzer* photometry. Poleski et al. (2016) and Zhu et al. (2017) have observed systematics on timescales of tens of days. In principle, the *Spitzer* light curve could be affected by such systematics, but they cannot be recognized because the total duration of the light curve is short. However, Zhu et al. (2017), based on the *Spitzer* event sample that was uniformly analyzed in that work, concluded that such long-term systematic trends in the *Spitzer* photometry appear in $< 5\%$ of all cases. Therefore, there is a $< 5\%$ probability that systematics in the *Spitzer* photometry led to our current solution. The proper motion is 6.6 mas yr^{-1} (independent of the parallax measurement). Thus, the solution can be checked with adaptive optics observations at first light of next-generation, thirty-meter class telescopes. For example, in 2028 the source and lens will be separated by 79 mas, which is ~ 6 times the FWHM at 1.6 microns for a 30-m telescope, so easily resolved even though the source is a giant. If the lens really is a brown dwarf, no light should be detected. However, if the solution is wrong (e.g. due to unknown systematics), then the lens should be more massive, i.e. a star. In that case, light from the lens should be directly detected. Furthermore, if light is detected, this will also allow a check of the direction of the source-lens relative proper motion.

7. CONCLUSION

We present the analysis of the binary lensing event MOA-2016-BLG-231 that was observed from the ground and from *Spitzer*. Even though *Spitzer* did not cover caustic-crossing parts and it covered only partial wing parts of the light curve, we could determine the physical properties of the lens. It is found that the lens is a binary system composed of low-mass BDs with $M_1 = 21_{-5}^{+12} M_J$ and $M_2 = 9_{-2}^{+5} M_J$, and it is located in the Galactic disk $D_{\text{L}} = 2.85_{-0.50}^{+0.88}$ kpc. The BD binary is moving counter to the orbital motion of disk stars. This solution can be checked in the future with adaptive optics observations with thirty-meter class telescopes. This result shows how *Spitzer* plays a crucial role in short t_{E} BD events, despite the fact that it covered only the declining wing of the light curve in a relatively short event.

Work by S.-J. Chung was supported by the KASI (Korea Astronomy and Space Science Institute) grant 2018-1-830-02. Work by WZ, and AG were supported by AST-1516842 from the US NSF. WZ, IGS, and AG were supported by JPL grant 1500811. Work by C.H. was supported by grant 2017R1A4A1015178 of National Research Foundation of Korea. Work by C.R. was supported by an appointment to the NASA Postdoctoral Program at the Goddard Space Flight Center, administered by USRA through a contract with NASA. This research has made use of the KMTNet system operated by KASI and the data were obtained at three host sites of CTIO in Chile, SAAO in South Africa, and SSO in Australia. The MOA project is supported by JSPS KAKENHI Grant Number JSPS24253004, JSPS26247023, JSPS23340064, JSPS15H00781, JP16H06287, and JP17H02871. The OGLE has received funding from the National Science Centre, Poland, grant MAESTRO 2014/14/A/ST9/00121 to A.U.

REFERENCES

- Alard, C., & Lupton, R. H. 1998, ApJ, 503, 325
 Albrow, M. D., Horne, K., Bramich, D. M., et al. 2009, MNRAS, 397, 2099
 Albrow, M. D., Yee, J. C., Udalski, A., et al. 2018, ApJ, 858, 107
 An, J. H., Albrow, M. D., Beaulieu J.-P., et al. 2002, ApJ, 572, 521
 Batista, V., Gould, A., Dieters, S., et al. 2011, A&A, 529, 102
 Bensby, T., Adén, D., Meléndez, et al. 2011, A&A, 533, 134
 Bessell, M. S., & Brett, J. M. 1988, PASP, 100, 1134
 Boyd, D. F. A., & Whitworth, A. P. 2005, A&A, 430, 1059
 Calchi Novati, S., Gould, A., Yee, J. C., et al. 2015, ApJ, 814, 92
 Choi, J.-Y., Han, C., Udalski, A., et al. 2013, ApJ, 768, 129
 Claret, A. 2000, A&A, 363, 1081
 Claret, A., & Bloemen, S. 2011, A&A, 529, A75
 Gould, A. 1992, ApJ, 392, 442
 Gould, A. 1994, ApJ, 421, L75
 Gould, A. 2000, ApJ, 542, 785
 Gould, A. 2008, ApJ, 681, 1593
 Gould, A. 2013, ApJ, 763, L35

- Han, C., Jung, Y. K., Udalski, A., et al. 2013, *ApJ*, 778, 38
Han, C., Jung, Y. K., Udalski, A., et al. 2016, *ApJ*, 822, 75
Han, C., Udalski, A., Bozza, V., et al. 2017, *ApJ*, 843, 87
Han, C., Udalski, A., Sumi, T., et al. 2017, *ApJ*, 843, 59
Jung, Y. K., Udalski, A., Sumi, T., et al. 2015, *ApJ*, 798, 123
Kayser, R., Refsdal, S., & Stabell, R. 1986, *A&A*, 166, 36
Kervella, P., Thévenin, F., Di Folco, E., Ségransan, D. 2004, *A&A*, 426, 297
Kim, H.-W., Hwang, K.-H., Kim, D.-J., et al. 2018, *AAS* submitted, arXiv:1804.03352
Kim, S.-L., Lee, C.-U., Park, B.-G., et al. 2016, *JKAS*, 49, 37
Nataf, D. H., Gould, A., Fouqué, P., et al. 2013, *ApJ*, 769, 88
Park, H., Udalski, A., Han, C., et al. 2013, *ApJ*, 778, 134
Park, H., Udalski, A., Han, C., et al. 2015, *ApJ*, 805, 117
Pejcha, O., & Heyrovský D. 2009, *ApJ*, 690, 1772
Poleski, R., Zhu, W., Christie, G. W., et al. 2016, *ApJ*, 823, 63
Ranc, C., Cassan, A., Albrow, M. D., et al. 2015, *A&A*, 580, 125
Refsdal, S. 1966, *MNRAS*, 134, 315
Reipurth, B., Clarke, C. 2001, *AJ*, 122, 432
Rhie, S. H., Becker, A. C., Bennett, D. P. 1999, *ApJ*, 522, 1037
Ryu, Y.-H., Udalski, A., Yee, J. C., et al. 2017, *AJ*, 154, 247
Schechter, P. L., Mateo, M., Saha, A. 1993, *PASP*, 105, 1342
Schneider, P., & Weiss, A. 1988, *ApJ*, 330, 1
Shin, I.-G., Han, C., Gould, A., et al. 2012, *ApJ*, 760, 116
Shin, I.-G., Udalski, A., Yee, J. C., et al. 2017, *AJ*, 154, 176
Shvartzvald, Y., Li, Z., Udalski, A., et al. 2016, *ApJ*, 831, 183
Shvartzvald, Y., Yee, J. C., Calchi Novati S., et al. 2017, *ApJ*, 840, L3
Shvartzvald, Y., Yee, J. C., Skowron J., et al. 2018, arXiv:1805.08778
Siverd, R. J., Beatty, T. G., Pepper, J., et al. 2012, *ApJ*, 761, 123
Skowron J., Udalski, A., Gould, A., et al. 2011, *ApJ*, 738, 87
Stamatellos, D., Hubber, D. A., & Whitworth, A. P. 2007, *MNRAS*, 382, L30
Street, R. A., Choi, J.-Y., Tsapras, Y., et al. 2013, *ApJ*, 763, 67
Suzuki, D., Bennett, D. P., Sumi, T., et al. 2016, *ApJ*, 833, 145
Udalski, A. 2003, *AcA*, 53, 291
Udalski, A., Yee, J. C., Gould, A., et al. 2015, *ApJ*, 799, 237
Wambsganss, J. 1997, *MNRAS*, 284, 172
Whitworth, A. P., Zinnecker, H. 2004, *A&A*, 427, 299
Yee, J. C., Gould, A., Beichman, C., et al. 2015, *ApJ*, 810, 155
Yoo, J., DePoy, D. L., Gal-Yam, A., et al. 2004, *ApJ*, 603, 139
Zhu, W., Udalski, A., Calchi Novati, S., et al. 2017, *AJ*, 154, 210
Zhu, W., Udalski, A., Gould, A., et al. 2015, *ApJ*, 805, 8

Table 1
Microlensing brown dwarfs in binaries.

Event	M_{host} (M_{\odot})	M_{comp} (M_J)	D_L (kpc)	t_E (days)	μ (mas/yr)	π_E^\dagger	Reference
OGLE-2006-BLG-277	0.10 ± 0.03	52 ± 15	0.60 ± 0.14	37.9 ± 0.1	13.0 ± 1.1	1.13 ± 0.16	(1)
MOA-2007-BLG-197 ^(a)	0.82 ± 0.04	41 ± 2	4.17 ± 0.30	82.3 ± 1.2	4.0 ± 0.2	—	(2)
OGLE-2009-BLG-151	0.018 ± 0.001	7.9 ± 0.3	0.39 ± 0.01	28.0 ± 0.1	9.3 ± 0.1	3.45	(3)
MOA-2010-BLG-073	0.16 ± 0.03	11.0 ± 2.0	2.8 ± 0.4	44.3 ± 0.1	4.6 ± 0.4	0.37	(4)
OGLE-2011-BLG-0420	0.025 ± 0.001	9.9 ± 0.5	1.99 ± 0.08	35.2 ± 0.1	3.4 ± 0.3	1.17	(3)
MOA-2011-BLG-104	0.18 ± 0.11	21 ± 10	3.29 ± 1.20	39.3 ± 0.5	5.0 ± 0.7	0.34 ± 0.21	(5)
MOA-2011-BLG-149	0.14 ± 0.02	20 ± 2	1.07 ± 0.10	179.7 ± 8.5	2.1 ± 0.2	0.78 ± 0.04	(5)
OGLE-2012-BLG-0358	0.022 ± 0.002	1.9 ± 0.2	1.73 ± 0.12	26.5 ± 0.1	4.0 ± 0.4	1.50	(6)
OGLE-2013-BLG-0102	0.10 ± 0.01	12.6 ± 2.1	3.04 ± 0.31	37.6 ± 0.4	4.2 ± 0.4	0.48	(7)
OGLE-2013-BLG-0578	0.12 ± 0.01	33.5 ± 4.2	1.16 ± 0.11	72.1 ± 0.8	4.9 ± 0.4	0.77	(8)
OGLE-2014-BLG-0257	0.19 ± 0.02	37.7 ± 5.2	1.25 ± 0.13	77.9 ± 1.4	5.3 ± 0.4	0.60	(9)
OGLE-2014-BLG-1112	1.07 ± 0.28	31.8 ± 8.2	4.84 ± 0.67	106.4 ± 0.9	3.2 ± 0.5	0.08	(10)
OGLE-2015-BLG-1319 ^(b)	0.60 ± 0.07	59.1 ± 4.1	4.84 ± 0.13	98.8 ± 4.7	2.4 ± 0.2	0.12	(11)
OGLE-2016-BLG-0693	0.86 ± 0.24	42.9 ± 16.5	4.85 ± 0.67	142.3 ± 49.9	1.7 ± 0.4	0.09	(12)
OGLE-2016-BLG-1195 ^(c)	0.08 ± 0.01	0.004 ± 0.001	3.91 ± 0.42	10.0 ± 0.1	10.5 ± 1.4	0.44	(13)
OGLE-2016-BLG-1469	0.05 ± 0.01	13.6 ± 2.1	4.47 ± 0.51	99.7 ± 0.8	0.9 ± 0.1	0.43	(14)
OGLE-2016-BLG-1266 ^(d)	0.016 ± 0.002	11.8 ± 0.7	3.03 ± 0.19	8.68 ± 0.08	9.4 ± 0.5	1.01 ± 0.09	(15)

Note. — M_{host} and M_{comp} are the masses of the host and companion, respectively. Except (a), (b), (c), and (d), the masses of 13 binary lens systems are obtained from ground-based parallax measurements. For the (a), the lens mass is obtained based on the fluxes and colors of the source, while for the (b) and (c), it is obtained from space-based parallax measurements. \dagger For errors of π_E , only values provided in each paper are presented. This is because for cases of providing only errors of $\pi_{E,N}$ and $\pi_{E,E}$, it is not clear that the correlation between $\pi_{E,N}$ and $\pi_{E,E}$ is linear or not. If the correlation is not linear like the event MOA-2016-BLG-231, it is difficult to estimate the error of π_E .

References. (1) Park et al. (2013), (2) Ranc et al. (2015), (3) Choi et al. (2013), (4) Street et al. (2013), (5) Shin et al. (2012), (6) Han et al. (2013), (7) Jung et al. (2015), (8) Park et al. (2015), (9) Han et al. (2016), (10) Han et al. (2017a), (11) Shvartzvald et al. (2016), (12) Ryu et al. (2017), (13) Shvartzvald et al. (2017), (14) Han et al. (2017b), and (15) Albrow et al. (2018).

Table 2
Lensing parameters.

Parameter	Best-fit solutions		Four models with $\Delta\chi^2 \sim 9$ from Figs. 4 & 5.			
	(+, -)	(-, -)	model 1	model 2	model 3	model 4
χ^2/dof	1274.14/1261	1276.06/1261	1282.396/1261	1282.399/1261	1282.951/1261	1283.129/1261
t_0 (HJD')	7534.6227 ± 0.0268	7534.6419 ± 0.0249	7534.6442	7534.6031	7534.6157	7534.6284
u_0	0.1976 ± 0.0037	-0.1960 ± 0.0036	0.1934	0.1995	0.1987	0.1947
t_E (days)	12.9168 ± 0.1006	12.9902 ± 0.1188	12.9337	13.0267	13.0604	12.9333
s	1.3251 ± 0.0040	1.3260 ± 0.0042	1.3235	1.3294	1.3294	1.3242
q	0.4258 ± 0.0080	0.4163 ± 0.0080	0.4167	0.4251	0.4218	0.4219
α (rad)	4.2705 ± 0.0036	-4.2741 ± 0.0035	4.2745	4.2683	4.2724	4.2726
ρ	0.0312 ± 0.0005	0.0306 ± 0.0005	0.0309	0.0309	0.0307	0.0313
$\pi_{E,N}$	-0.7598 ± 0.3156	-0.4996 ± 0.3047	-0.0896	-0.8265	-1.0557	-1.5830
$\pi_{E,E}$	-0.2283 ± 0.1370	-0.1749 ± 0.1219	-0.1325	-0.1777	-0.4287	-0.6839
ds/dt (yr ⁻¹)	-0.4685 ± 0.2488	-0.2251 ± 0.2943	-0.5464	-0.3029	-0.2988	-0.6677
$d\alpha/dt$ (yr ⁻¹)	-0.5675 ± 0.3229	1.2918 ± 0.3137	-1.1243	-0.4856	-0.6642	-0.5712
$f_{s,\text{spitz}}$	53.0998 ± 1.1631	51.6615 ± 1.5408	52.7683	52.3067	50.3992	52.9877
$f_{b,\text{spitz}}$	-4.5176 ± 1.1751	-2.9948 ± 1.5462	-4.1389	-3.5522	-2.1597	-4.5540
$f_{s,\text{ogle}}$	9.0629 ± 0.1684	8.8468 ± 0.1975	8.9815	8.9539	8.8901	9.0908
$f_{b,\text{ogle}}$	0.3316 ± 0.1677	0.5470 ± 0.1966	0.4127	0.4393	0.5024	0.3020

Note. — HJD' = HJD - 2450000.

Table 3
Physical lens parameters.

Parameter	(+, -)	(-, -)	model 1	model 2	model 3	model 4
$M_{\text{tot}} (M_{\odot})$	$0.029^{+0.016}_{-0.007}$	$0.037^{+0.028}_{-0.011}$	0.180	0.034	0.025	0.016
$M_1 (M_{\odot})$	$0.020^{+0.011}_{-0.005}$	$0.026^{+0.020}_{-0.008}$	0.127	0.024	0.018	0.012
$M_2 (M_{\odot})$	$0.009^{+0.005}_{-0.002}$	$0.011^{+0.008}_{-0.003}$	0.053	0.010	0.008	0.005
a_{\perp} (au)	$0.88^{+0.27}_{-0.15}$	$1.03^{+0.36}_{-0.21}$	1.96	0.98	0.80	0.59
D_L (kpc)	$2.85^{+0.88}_{-0.5}$	$3.33^{+1.16}_{-0.67}$	6.33	3.14	2.57	1.93
$(\text{KE/PE})_{\perp}$	$0.16^{+0.20}_{-0.10}$	$0.52^{+0.30}_{-0.21}$	0.76	0.10	0.13	0.09
$\mu_{L,\text{hel,N}}$ (mas yr $^{-1}$)	$-6.16^{+0.40}_{-0.38}$	$-6.09^{+0.43}_{-0.39}$	-3.67	-6.35	-6.01	-5.87
$\mu_{L,\text{hel,E}}$ (mas yr $^{-1}$)	$-0.37^{+0.25}_{-0.39}$	$-0.87^{+0.34}_{-0.74}$	-5.03	-0.03	-0.72	-0.10
$v_{L,\text{pec,l}}$ (km s $^{-1}$)	$-144.12^{+37.69}_{-50.40}$	$-172.29^{+38.72}_{-66.15}$	-331.79	-160.13	-129.25	-90.08
$v_{L,\text{pec,b}}$ (km s $^{-1}$)	$-27.78^{+5.95}_{-7.79}$	$-24.98^{+7.17}_{-7.71}$	85.82	-38.37	-20.73	-18.29

Note. — Physical lens parameters for (+, -) and (-, -) solutions represent the median values of each physical parameter from the (+, -) and (-, -) MCMC chains, and their error bars represent the 16th and 84th percentile values of each physical parameter from the chains. This is because the correlation between $\pi_{E,N}$ and $\pi_{E,E}$ components is not well approximated by a linear relation, as shown in Figure 4.

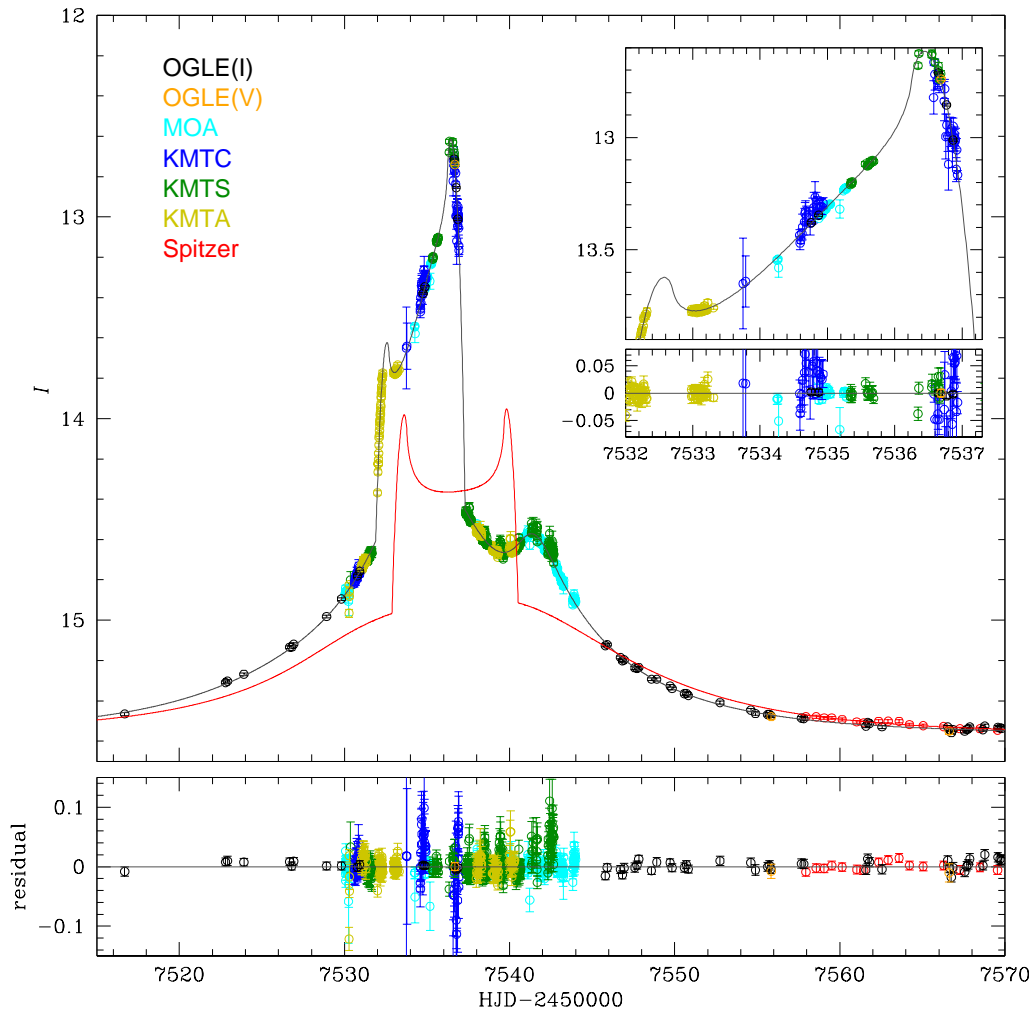


Figure 1. Light curves of the best-fit binary model, (+, -) model, for MOA-2016-BLG-231, including both microlens parallax and orbital effects. Black and red lines represent the light curves as seen from Earth and *Spitzer*, respectively.

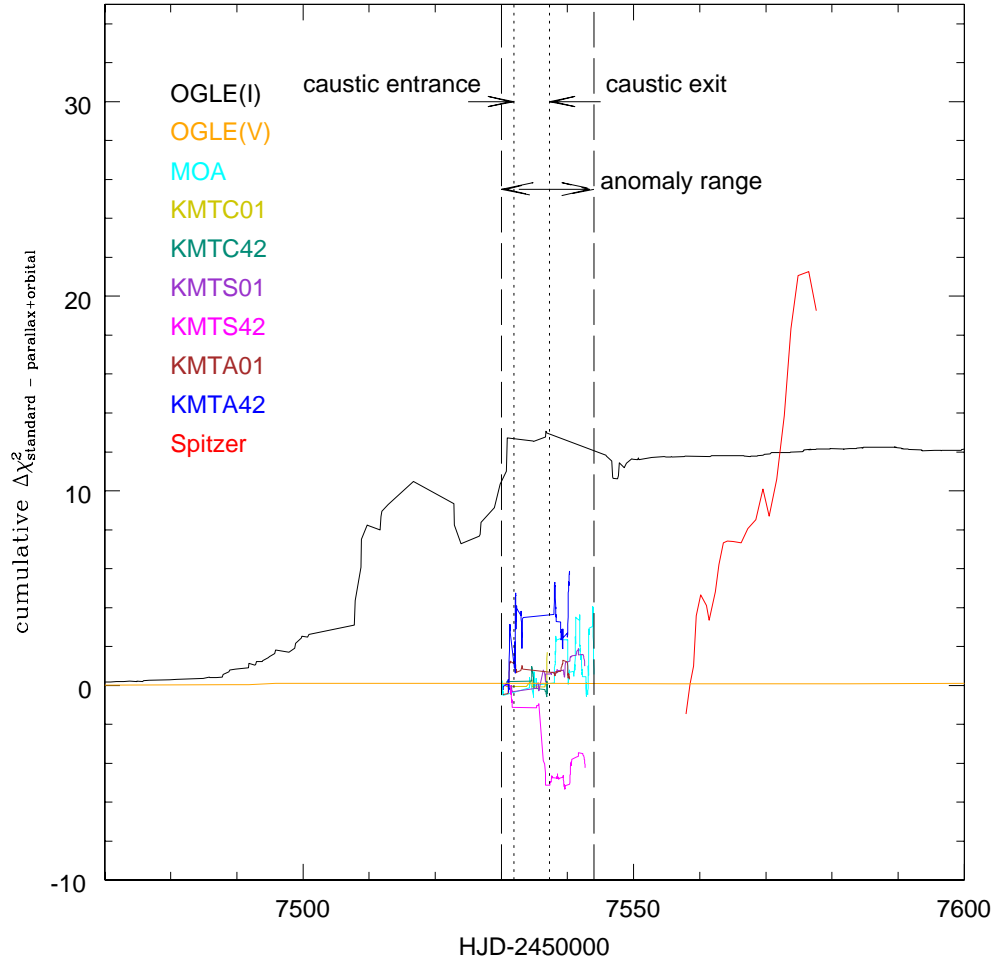


Figure 2. Cumulative distribution of $\Delta\chi^2$ between the standard and the parallax+orbital models for (+, -). All ground-based data except OGLE are used only in the anomaly range $7530.0 < \text{HJD} - 2450000 \text{ (HJD')} < 7544.0$. The epochs of the entrance and exit of the caustic are $\text{HJD}' = 7531.9$ and 7537.3 , respectively.

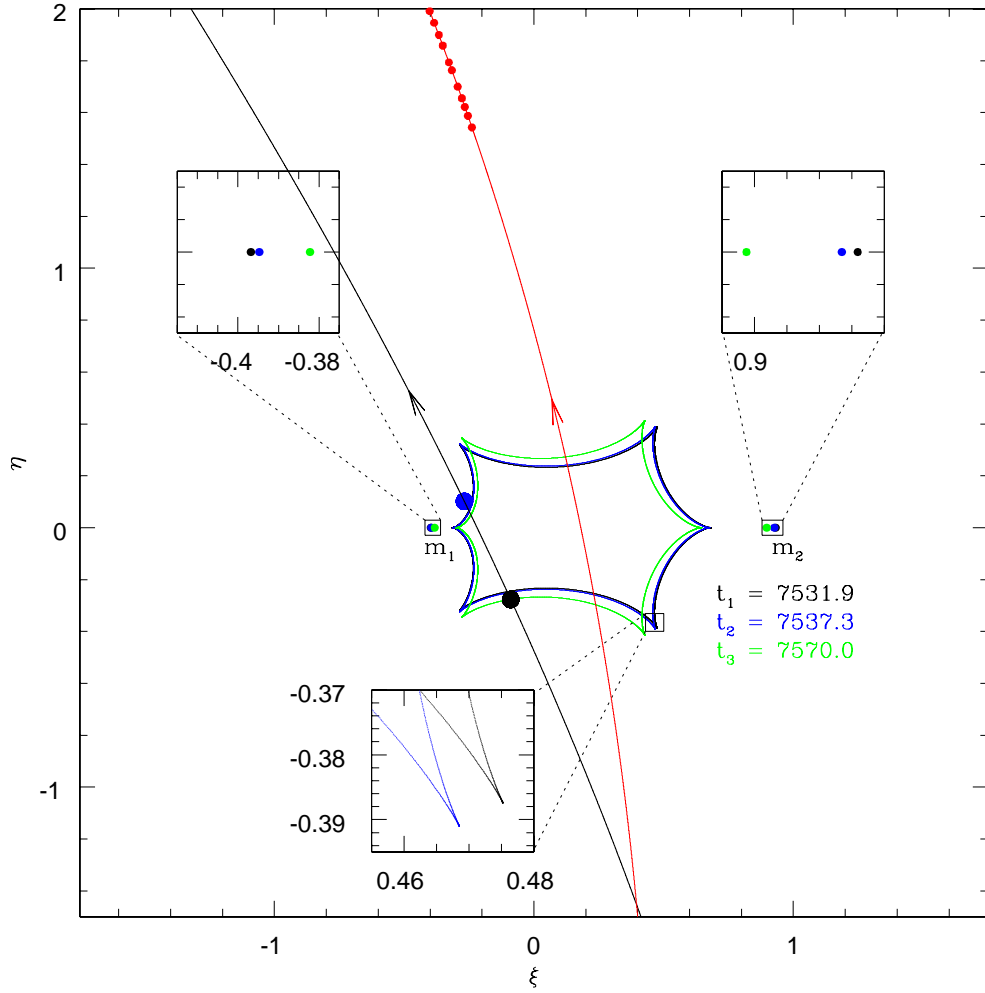


Figure 3. Source trajectories for the best-fit (+, -) model as seen from the ground (black) and *Spitzer* (red), with the red points indicating the epochs of *Spitzer* data. The caustic structure and positions of the binary lens components change with time due to the lens orbital motion, and these changes are shown at three epochs, $t_1 = 7531.9$ (caustic entrance), $t_2 = 7537.3$ (caustic exit), and $t_3 = 7570.0$ (close to baseline). However, the caustic and lens components at the two epochs t_1 and t_2 overlap and so require zooms to see these effects (see insets). The black and blue solid circles on the caustic curve represent the source positions at t_1 and t_2 , respectively. M_1 and M_2 are the primary and secondary components of the binary.

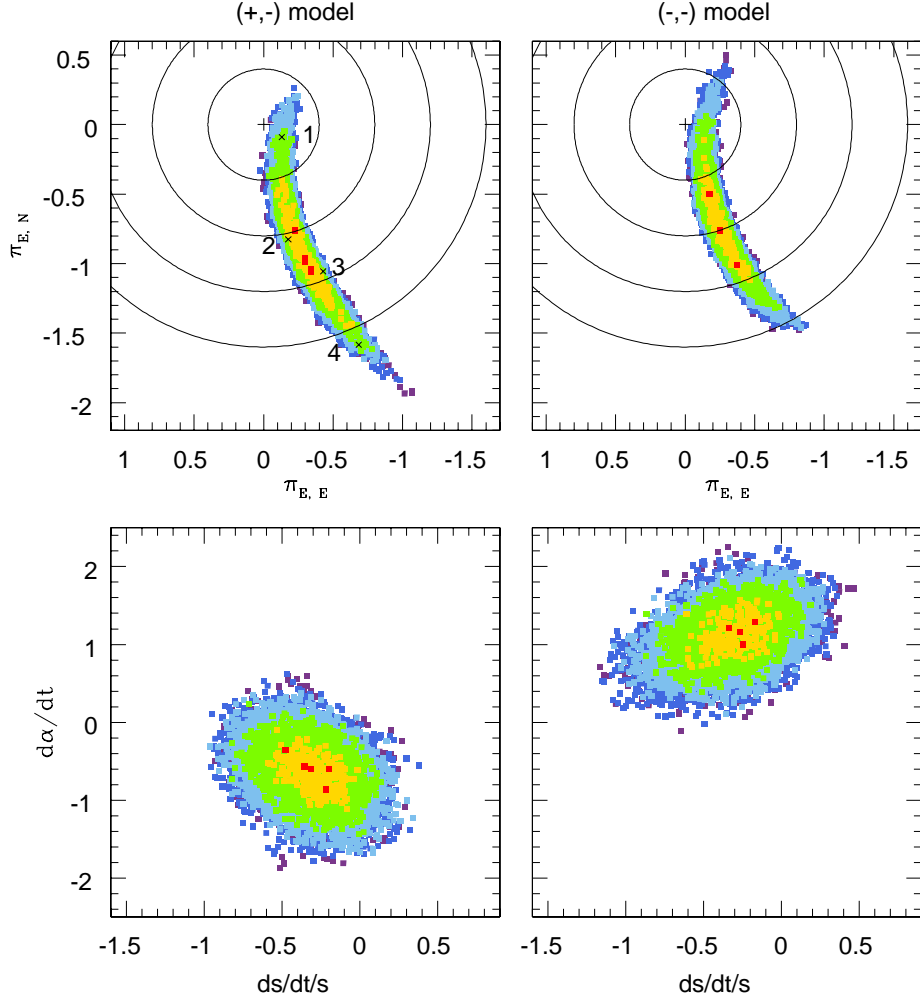


Figure 4. $\Delta\chi^2$ distributions of the microlens parallax and orbital motion parameters for the two best-fit models obtained from the parallax+orbital modeling. The red, yellow, green, light blue, dark blue, and purple colors represent regions with $\Delta\chi^2 < (1, 4, 9, 16, 25, 36)$, from the best-fit model, respectively. The four solid circles in the parallax distributions are centered at $(\pi_{E,N}, \pi_{E,E}) = (0, 0)$ and have the radii of $\pi_E = (0.4, 0.8, 1.2, 1.6)$, respectively. Four parallax models, which are located inside the 3σ contour, are marked as 1, 2, 3, and 4 in the distribution of the $(+,-)$ model. The trajectories and light curves for these four models are illustrated in Figure 5.

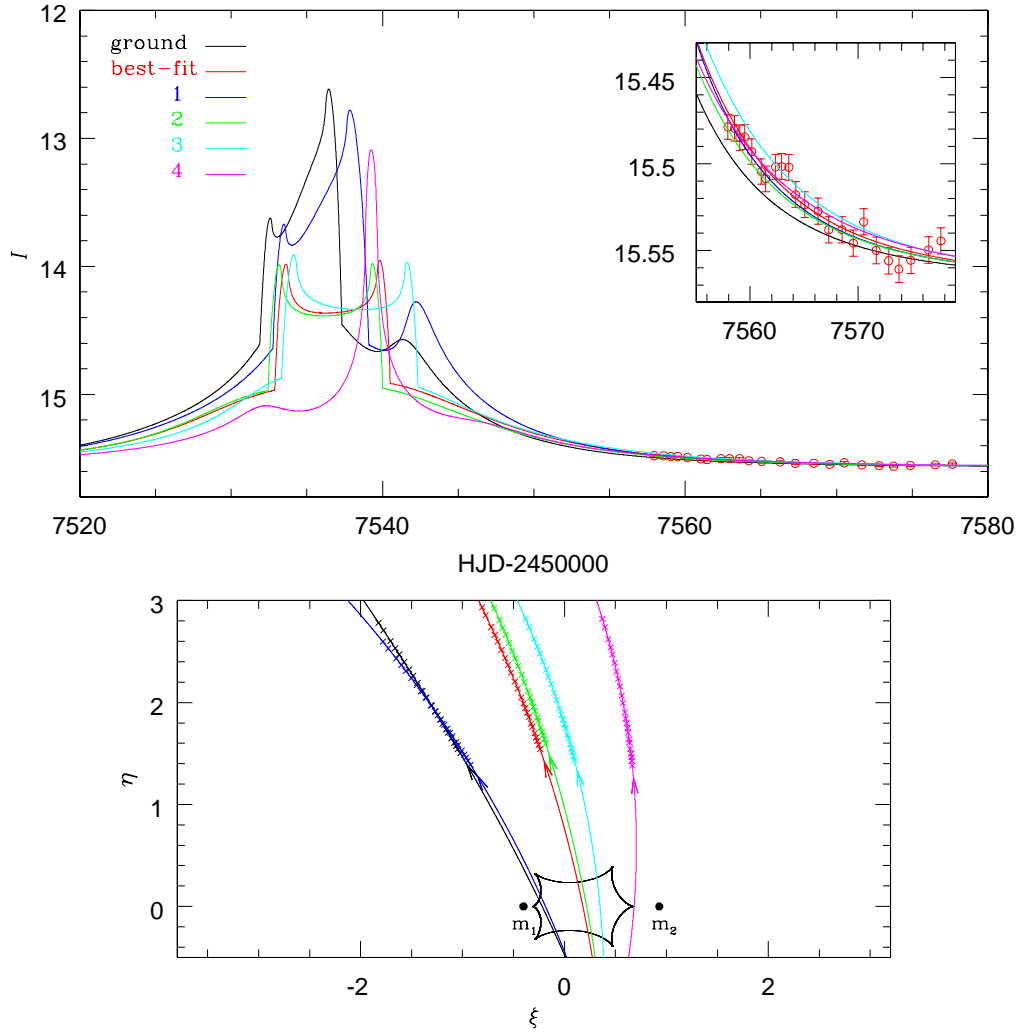


Figure 5. Upper panel : *Spitzer* light curves for the best-fit model and the four $\Delta\chi^2 \sim 9$ models highlighted in Figure 4. Each model is drawn with different colors. The black curve represents the best-fit ground-based light curve. The *Spitzer* data are plotted on the best-fit light curve. Bottom panel : Corresponding *Spitzer* and ground-based trajectories. They are drawn with the same color as in the upper panel.

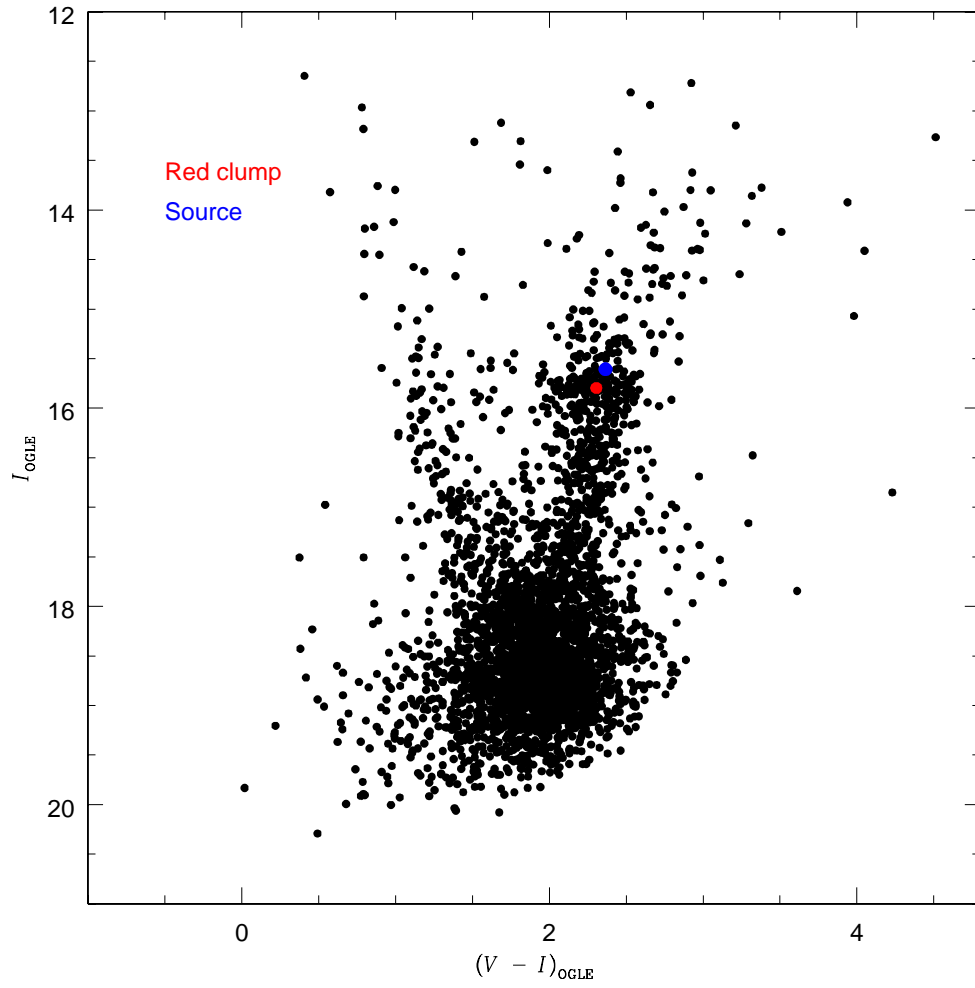


Figure 6. Instrumental color-magnitude diagram (CMD) of stars in the observed field. The red and blue circles mark the centroid of the red clump giant and microlensed source star, respectively.

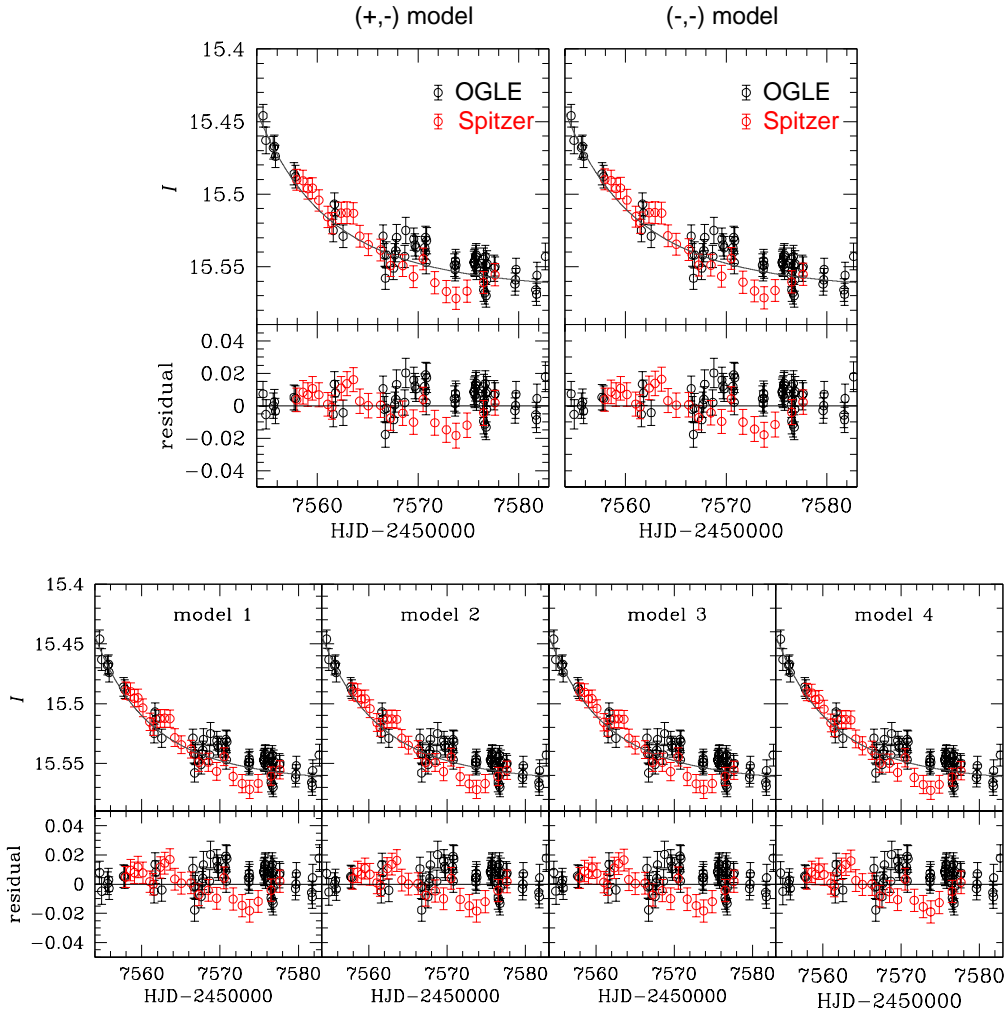


Figure 7. Light curves for the standard model, which is conducted under the conditions that the high-order effect parameters are set to zero and the initial values of the other standard model parameters including *Spitzer* fluxes are set to the best-fit solutions of (+, -) and (-, -) models (Upper panel) and the solutions of four models indicated in Figure 4 (Bottom panel).

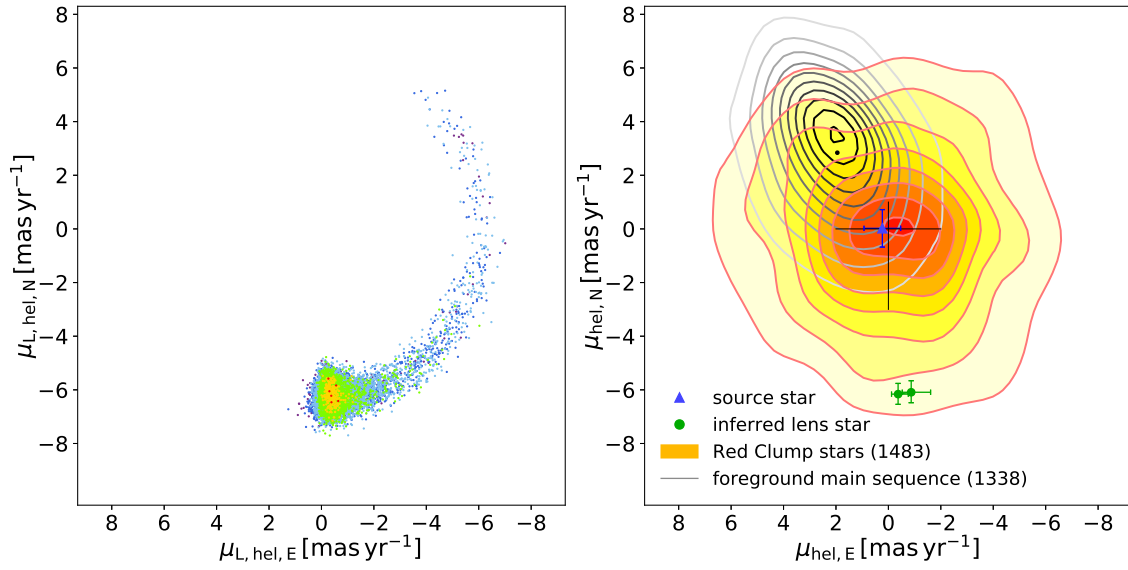


Figure 8. Left panel: Scatter of the heliocentric proper motion of the lens for the $(+, -)$ best-fit model. The color notation is the same as Figure 4. Right panel: Proper motion of stars in the observed field within a $6.5' \times 6.5'$ square. Orange and grey contours represent the proper motions of red clump stars and main sequence stars, which correspond to the bulge and disk populations, respectively. The blue triangle is the proper motion of the source, while the green dots are the lens proper motions of two degenerate solutions, $(+, -)$ and $(-, -)$. The source is essentially at rest with respect to the bulge stars.